

Accepted Manuscript

Title: Synthesis, Characterisation, and Catalytic Properties of Halloysite-Supported Metal Nanoparticles

Authors: Jacob. E. Jaïne, Michael. R. Mucalo

PII: S0025-5408(17)34330-1
DOI: <https://doi.org/10.1016/j.materresbull.2018.11.027>
Reference: MRB 10283

To appear in: *MRB*

Received date: 19 November 2017
Revised date: 9 August 2018
Accepted date: 20 November 2018



Please cite this article as: Jaïne JE, Mucalo MR, Synthesis, Characterisation, and Catalytic Properties of Halloysite-Supported Metal Nanoparticles, *Materials Research Bulletin* (2018), <https://doi.org/10.1016/j.materresbull.2018.11.027>

This is a PDF file of an unedited manuscript that has been accepted for publication. As a service to our customers we are providing this early version of the manuscript. The manuscript will undergo copyediting, typesetting, and review of the resulting proof before it is published in its final form. Please note that during the production process errors may be discovered which could affect the content, and all legal disclaimers that apply to the journal pertain.

Synthesis, Characterisation, and Catalytic Properties of Halloysite-Supported Metal Nanoparticles

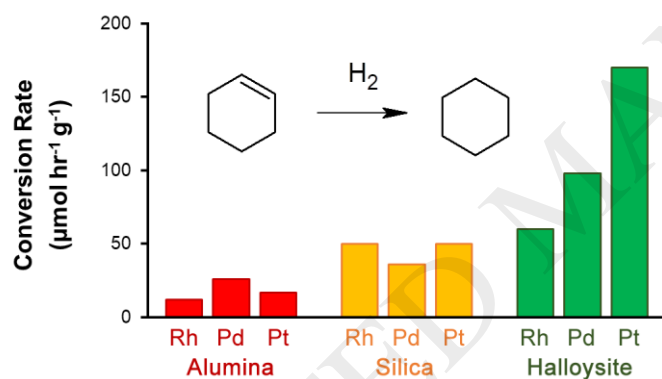
Authors: Jacob. E. Jaine (jacob.e.jaine@gmail.com)^{a,b}

Michael. R. Mucalo (michael.mucalo@waikato.ac.nz, corresponding author)^a

Affiliations: a) Chemistry, School of Science, Faculty of Science and Engineering, University of Waikato, New Zealand.

b) Analytica Laboratories, Ruakura Research Centre, Hamilton, New Zealand

Graphical Abstract



Highlights

- Metal nanoparticles were immobilised onto halloysite by a facile synthetic method
- The materials showed exceptional catalytic activity in several hydrogenations
- Halloysite-based catalysts were more active than alumina or silica equivalents
- The activity was found to be correlated with the spatial distribution of metal
- Spectroscopic analyses gave insight into the binding sites of the metal

Abstract

A facile synthetic method is reported for the immobilisation of metal nanoparticles on halloysite, an aluminosilicate material with a unique nanotubular structure. A one-step colloidal synthesis was developed, from which nine different catalysts were prepared. The materials were tested in three different catalytic hydrogenations, and the halloysite-supported catalysts were found to outperform alumina- or silica-supported catalysts prepared in the same fashion. Electron microscopy showed that the activity was closely linked to the spatial distribution of the supported metal particles, which in turn affected the shapes of certain surface-associated peaks in the infrared and nuclear magnetic resonance spectra. From this data insight is gained into the nature of the interaction between metal nanoparticles and the surfaces of these support materials.

Abbreviations

TOF – Turnover frequency

HNC – Halloysite nanotubes

TEM – Transmission electron microscopy

SEM – Scanning electron microscopy

EDS – Energy dispersive spectroscopy

BSD – Backscatter detector/detection

XRD – X-ray diffraction

NMR – Nuclear magnetic resonance (spectroscopy)

FTIR – Fourier transform infrared (spectroscopy)

ICDD – International centre for diffraction data

FWHM – Full width at half maximum

Key Words

A. Nanostructures, A. Surfaces, B. Microstructure, C. Electron microscopy, D. Catalytic properties

1. Introduction

Halloysite nanoclay (abbreviated 'HNC') is a naturally occurring aluminosilicate clay with a unique tubular microstructure. It is composed of alternate layers of octahedral alumina and tetrahedral silica sheets, which have an intrinsic 'lateral misfit'. This produces a stress across the sheets, which is relieved by rolling into tubular crystals [1]. The resulting nano-sized tubules have an alumina-rich interior, and a silica-rich exterior. Substitution of the structural Al^{3+} ions for Fe^{3+} ions enlarges the octahedral alumina sheets, which relieves the stress and produces halloysite particles with a flatter morphology [2]. The surface area of halloysite ranges from $30 \text{ m}^2 \text{ g}^{-1}$ to $170 \text{ m}^2 \text{ g}^{-1}$ depending on the proportion of nanotubes, which account for the majority of the surface area [3]. It forms naturally by hydrothermal alteration of other clays throughout the world, though one of the purest sources is the Matauri Bay mine in Northland, New Zealand [4].

A range of applications have been found for halloysite [5, 6], including drug delivery [7, 8] or as a component of nanocomposites [9]. Importantly, its properties make it attractive as a support material for catalysts, especially metal nanoparticles [10, 11]. Recent studies have shown that halloysite is a viable support for many catalytic systems, with examples that include decomposition of chlorophenols by $\text{Fe}_3\text{O}_4/\text{HNC}$ [12], plasmonic photodegradation of dyes by Au/HNC [13], reduction of nitrophenols by Rh/HNC [10, 14]_ENREF_8, synthesis of propargylamines by Ag/HNC [15], hydrogen production by CdS/HNC [16], hydrogenation of phenol by Ru/HNC [17], oxidation of benzyl alcohol by Au/HNC [18], and several others [19-22].

A similar group of systems are metal nanoparticles supported on or confined within zeolites, which have been used in a range of reactions including hydrogenations. For example, Pd or Pt immobilised on zeolite has been used to hydrogenate olefins and nitro compounds [23], while Pt and Rh encapsulated in zeolite has been used for the chemoselective hydrogenation of cinnamaldehyde [24], Ru-loaded zeolite has been used for the hydrolytic hydrogenation of cellulose to hexitols [25], and bimetallic Ni-Pt nanoparticles immobilised on zeolite have been used for hydrogenating carbonyls [26]. While zeolites are a

group comprising a relatively broad range of structures, much of this work has been performed with the easily-synthesisable zeolite Y.

Though it is clear that natural aluminosilicates like halloysite have a promising role as catalyst supports, the benefits of halloysite over traditional support materials like silica or alumina are seldom investigated. Therefore, this communication describes the characterisation and activity of catalysts prepared using halloysite sourced from New Zealand's Matauri Bay Mine. A simple one-pot synthetic method was used to immobilise Rh, Pd, or Pt nanoparticles onto the surface of the halloysite, as well as the traditional support materials alumina and silica. The resulting materials were tested in the catalytic hydrogenation of three olefins, and then characterised by a suite of instrumental methods. Structure-activity relationships are drawn from the data, and used to derive insight into the binding of the metal particles.

2. Experimental

2.1 Preparation of Catalysts

Methods for synthesising supported catalysts have become increasingly complex and specialist [27], so we sought to develop a simple wet chemical method for this purpose. This involved reducing appropriate metal salts in a suspension of the support material, followed by precipitation of the colloidal material using a flocculant.

For the research described herein, 2.97 g of either SiO₂ (>99.9%, Merck), Al₂O₃ (>99.5%, BDH), or halloysite (Imerys) was suspended in solutions of either RhCl₃ (>99%, Precious Metals Online), Na₂PdCl₄ (>99%, Aldrich), or H₂PtCl₆ (>99.0%, BDH). Concentrations of the metal salts were set such that in 100 mL of solution there was 30 mg of each metal, so that when reduced, the catalysts would have a loading of 1.0 wt%. Reduction of the metal salts to their finely divided metallic form was brought about by dropwise addition of 5.00 mL of 0.05 mol L⁻¹ NaBH₄ solution (>99%, Ajax). During this period, the nascent nanoparticles could adsorb to the support materials, producing a supported catalyst.

After reduction, the suspensions were stirred for a further 30 minutes, followed by addition of 100 µL of 0.1 mol L⁻¹ LaCl₃ solution (>99.9%, Ajax) to destabilise any material remaining in colloidal suspension [28]. The resulting materials were gravity filtered, washed free of chloride and other residual salts, dried at 100°C in air, and then stored *in vacuo* until further analysis.

2.2 Hydrogenations

The catalytic activity of the materials were tested using olefin hydrogenation as a probe reaction. Three different olefins were hydrogenated, namely cyclohexene (>99% AppliChem), 1,5-cyclooctadiene ('1,5-COD', >99%, Aldrich), and 1-octene (>97%, Merck). All hydrogenations were performed in a glass stirred-tank batch reactor under 1 atm of H₂ (>99.99%, BOC) at a temperature of 20 ± 0.2 °C. In each reaction ca. 100 mg of catalyst was added to the reactor along with 5.00 mL of organic substrate, and 45.0 mL of n-heptane as a solvent, chosen due to its favourable wetting properties [29]. Reactions were typically run for 90 minutes, and progress was monitored every 10 minutes by withdrawing 100 µL aliquots of the mixture through a rubber septum, diluting to 0.2 mg mL⁻¹ with acetone, and analysing by gas chromatography. All volumes, masses, and times were chosen to operate the reactions at high substrate concentrations and low conversion rates as appropriate for kinetic measurements.

All gas chromatographic analyses were performed using a Hewlett Packard 6890 gas chromatograph with 5972 mass-selective detector. Samples were injected (1 µL) onto a Zebtron ZB-5 capillary column at 50°C using a 1:100 split, and run isothermally using helium carrier gas at 1.0 mL min⁻¹, with a total programme length of 3 minutes. Normalisation was performed relative to the heptane peak area, and absolute concentrations obtained by interpolation from a standard curve.

2.3 Instrumental Characterisation

The pristine support materials and the metal-containing catalysts were analysed by a suite of instrumental methods. The spectra were then compared to determine the physical and chemical effects of immobilising metal particles onto the supports, and related to the catalytic activity of the systems to explore structure-activity relationships.

Morphological and textural characteristics of the materials were evaluated by scanning electron microscopy (SEM). All analyses were performed using a Hitachi S-4700 SEM equipped with a Thermo energy dispersive spectrometer (EDS) and a Hitachi backscatter detector (BSD). Powders were mounted on double-sided carbon tape on an aluminium stub and analysed in BSD mode, then sputtered with Pt and re-analysed in secondary electron mode.

Size distributions of the supported metal particles were measured by high-resolution transmission electron microscopy (TEM). All analyses were performed using a Philips CM30 operated at 250 kV. Samples were prepared by dispersing 10 mg of sample in 10 mL of water and sonicating for 10 seconds, followed by depositing 10 μ L on carbon/formvar-coated copper grids (ProSciTech Pty. Ltd.) and drying in air. Magnification calibrations were performed using bovine catalase (EMS Ltd.).

Crystallographic properties of the supports and catalysts were analysed by X-ray diffraction (XRD). All analyses were performed using a PANalytical Empyrean diffractometer with Ni-filtered Cu radiation. Diffractograms were each collected over an eight-hour period, covering the 2θ range 10° - 90° in 0.013° steps. Samples were prepared by backloading, and spun at 1 Hz during acquisition. Pattern matching was performed using HighScore Plus. As a secondary particle size measurement method, line broadening analysis was carried out on the patterns of the catalysts using the Scherrer equation, which relates the breadth of a diffraction peak to the size of the crystallites from which it originates. Using HighScore Plus, backgrounds were manually subtracted from the patterns using a cubic spline, and Voigt peaks fitted to the resulting profiles. The breadths were corrected for instrumental broadening by subtracting the peak widths of a CeO_2 standard prepared according to the literature [30]. All visible metal peaks were used during fitting, which typically included the (111), (200), (220), and (311) diffraction peaks, and a shape factor (K) of 0.9 was used in the calculation.

The bulk chemical structure of the materials were investigated by ^1H , ^{27}Al , and ^{29}Si solid-state nuclear magnetic resonance spectroscopy (NMR). All analyses were performed on a Bruker AVANCE 300 MHz spectrometer with a standard 4 mm H/X solids probe. Spectra were typically recorded with 90° pulses, spectral widths of 200 ppm, 30 ms acquisition times and varied recycle delays and numbers of transients depending on the nucleus being examined.

Finally, the bulk and surface vibrational properties of the materials were investigated by Fourier transform infrared spectroscopy (FTIR). Samples were prepared as KBr discs and analysed using a PerkinElmer Spectrum 200 FT spectrometer. Additionally, samples were analysed as neat powders by infrared microspectroscopy using a PerkinElmer Spotlight 200 FT microscope (yielding so-called 'MicroFTIR' or 'transflection' spectra). By virtue of this particular optical configuration it was considered that this method may be more surface-

sensitive than the traditional transmission/KBr disc method, and thus appropriate for studying surface-active systems like those described herein.

3. Results

3.1 Catalytic Activity

When the catalysts were loaded into the reactor under hydrogen, conversion of the substrate molecules began immediately and proceeded linearly throughout the 90-minute reactions. This was observed for all of the systems containing metal nanoparticles, but not for any of the support materials without metal nanoparticles. The conversion rates observed varied depending on the metal, the support material, and the substrate, as shown in Table 1.

Table 1: Measured catalytic activity of the thirty-six systems studied herein, expressed as the number of micromoles of substrate converted to product per hour per gram of catalyst. All rates are given to two significant figures.

Catalyst	Measured Activity ($\mu\text{mol hr}^{-1} \text{g}^{-1}$)		
	Cyclohexene	1-Octene	1,4-Cyclooctadiene
Rh/SiO ₂	50	180	36
Rh/Al ₂ O ₃	12	87	17
Rh/HNC	60	250	66
Pd/SiO ₂	36	130	34
Pd/Al ₂ O ₃	26	200	30
Pd/HNC	98	340	66
Pt/SiO ₂	50	130	14
Pt/Al ₂ O ₃	17	63	6.0
Pt/HNC	170	300	24
SiO ₂ (pristine)	0.0	0.0	0.0
Al ₂ O ₃ (pristine)	0.0	0.0	0.0
HNC (pristine)	0.0	0.0	0.0

The hydrogenation of cyclohexene proceeded in all cases directly to cyclohexane, with no side products observed. In all cases the reaction rates were linear, and in all cases were largest with halloysite-supported metals. In the case of Pt/HNC, a ten-fold greater

hydrogenation rate was observed compared to Pt/Al₂O₃ and nearly four-fold higher than Pt/SiO₂. The same trend was observed with supported Rh or Pd, though to a lesser extent. These conversion rates compare favourably with previously reported cyclohexene hydrogenation catalysts [31-34], especially as the reactions reported herein were performed under standard conditions.

The hydrogenation of 1-octene also proceeded linearly, though significant isomerisation was observed with the supported palladium catalysts (ca. 10-50% relative to the rate of hydrogenation depending on the system). The hydrogenation rates were generally several times higher than for cyclohexene hydrogenation, with a maximum conversion rate of 340 $\mu\text{mol hr}^{-1} \text{g}^{-1}$ for the Pd/HNC catalyst. These rates are again significantly higher than for the equivalent alumina- or silica-supported catalysts, and are higher than any activity reported in the literature with the exception of the study of Adlim *et al.* [35].

Lesser activities were observed in the hydrogenation of 1,5-COD, though once again the halloysite-supported catalysts were several times more active than the equivalent silica- or alumina-supported catalysts. The production of cyclooctane was linear in all observed cases, the maximum conversion rate observed being 66 $\mu\text{mol hr}^{-1} \text{g}^{-1}$ with the Pd/HNC catalyst, which was twice the rate observed for the Al₂O₃- or SiO₂-supported systems. These represent some of the highest activities for 1,5-COD hydrogenation by heterogeneous platinum-group catalysts, with the exception of the remarkably high activity of the Pd/pumice catalysts reported by Deganello *et al.* [36]. Like with 1-octene, some degree of isomerisation was observed during the hydrogenation, with the products at 30 minutes containing an average of 5.0% 1,5-COD isomers for the Pt catalysts, 6.4% for the Rh catalysts, and a much higher 33.5% for the Pd catalysts. These trends are consistent with known differences in the substrate absorption mechanism between the three metals [37]. Comparatively the choice of support material had little effect on the amount of isomerisation, the only obvious trend being that the silica-supported catalysts showed the greatest amount of isomerisation amongst all three metals tested. These same trends were also true of the octene hydrogenation described previously.

3.2 Electron Microscopy

Analysis of the pristine alumina by scanning electron microscopy showed that it was composed of spherical agglomerates, with diameters of $63 \pm 31 \mu\text{m}$ and no pore system. Catalysts prepared from the alumina shared the same general morphological characteristics, but were speckled with clusters of material not present in the pristine support. Under backscatter conditions these clusters showed up as bright points, and point analysis by EDS showed strong emission peaks corresponding in energy to the $K\alpha$ emission lines of Rh, Pd, or Pt. Further analysis by transmission electron microscopy showed the clusters were composed of spherical nanoparticles 3.3- 9.7 nm in diameter, as shown in Table 2. In addition to these clusters, inspection of the edges of the support material showed it was uniformly coated in particles with a surface coverage in excess of *ca.* 50%. Micrographs for these systems, and others, are given in Figures 1 and 2.

Table 2: Sizes of the metal nanoparticles in the nine catalyst systems studied, as measured by TEM (mean \pm standard deviation) and XRD (mean only).

System	Particle Size [nm]	
	TEM	XRD
Rh/SiO ₂	3.5 \pm 0.5	4.0
Pd/SiO ₂	5.0 \pm 0.8	7.3
Pt/SiO ₂	3.6 \pm 0.6	6.3
Rh/Al ₂ O ₃	3.3 \pm 0.6	<3
Pd/Al ₂ O ₃	9.7 \pm 4.1	9.2
Pt/Al ₂ O ₃	4.0 \pm 1.0	7.3
Rh/HNC	3.7 \pm 0.8	3.0
Pd/HNC	8.3 \pm 2.8	5.3
Pt/HNC	3.2 \pm 0.6	5.2

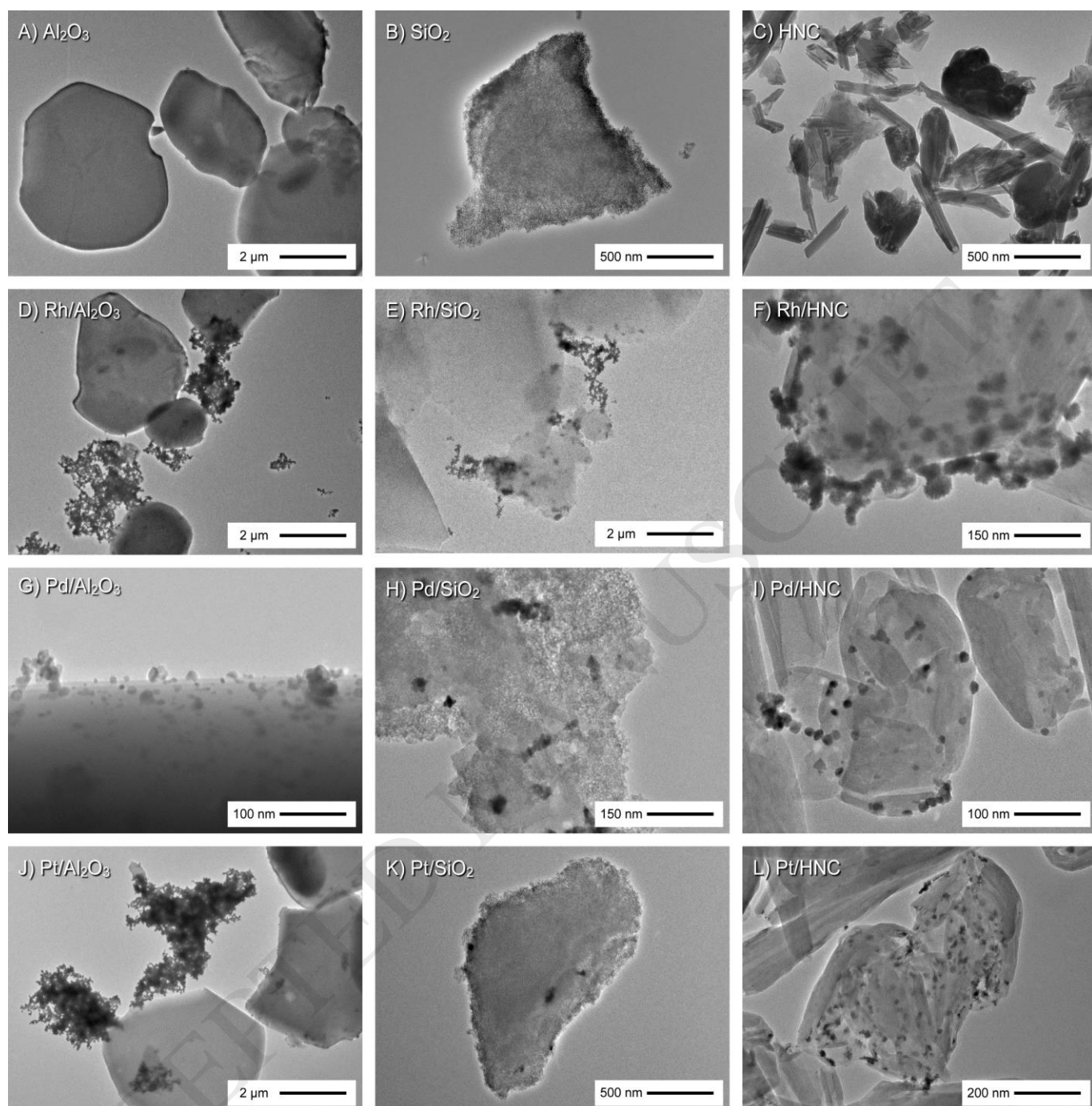


Figure 1: Transmission electron micrographs representing the systems studied herein. The top row shows the pristine support materials, while the remaining three rows show the catalysts containing immobilised nanoparticles.

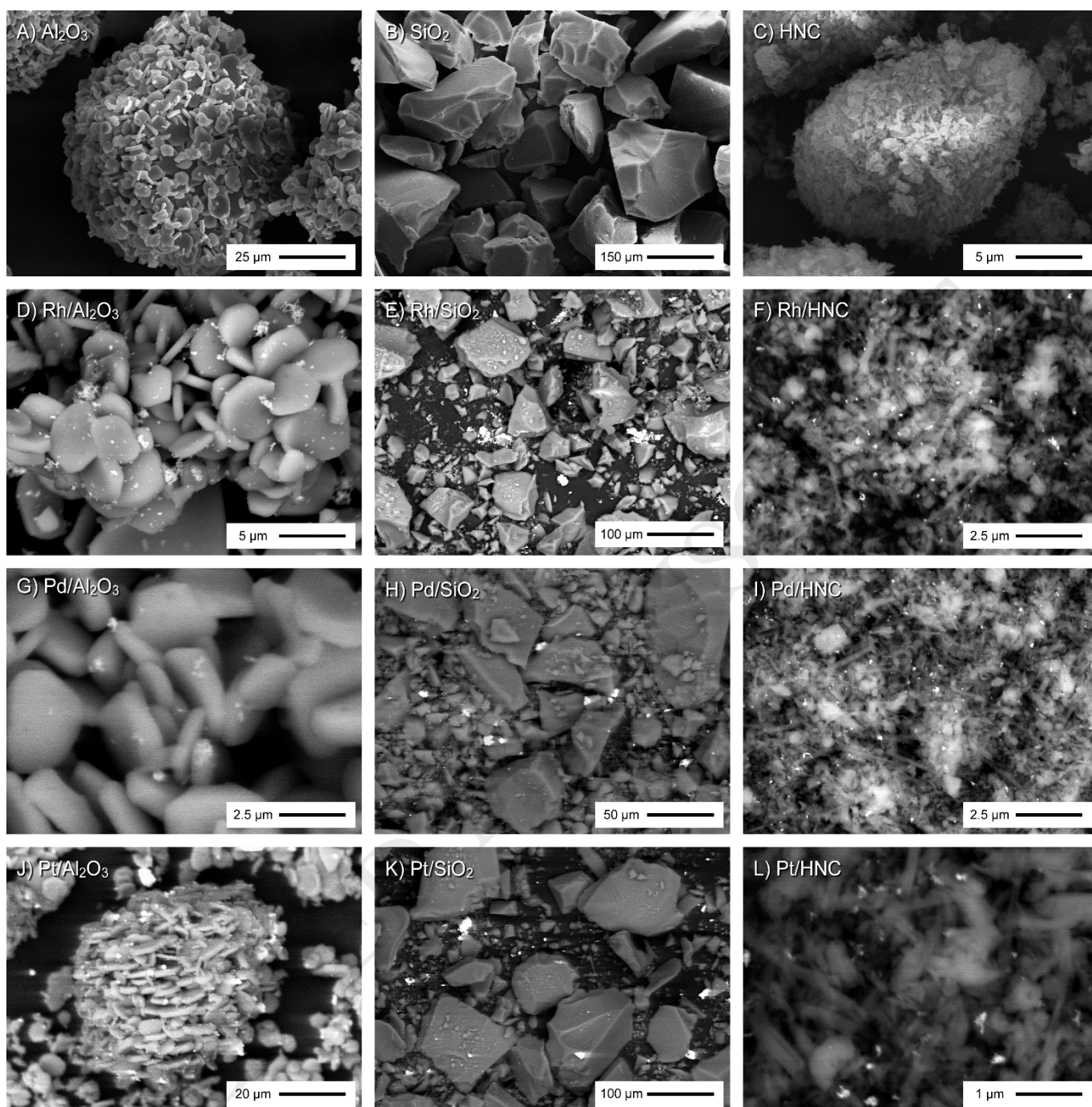


Figure 2: Scanning backscatter electron micrographs representing the twelve different systems studied herein. The top row shows the pristine support materials, while the remaining three rows show the catalysts containing immobilised nanoparticles.

Similar analyses of the pristine silica showed that it was composed of angular mesoporous particles with diameters of $94 \pm 40 \mu\text{m}$, which were present as discrete particles rather than

aggregates. Under backscatter conditions the same bright flecks were observed, as well as the same sets of emission lines *via* EDS. Analysis by transmission electron microscopy showed the clusters were also composed of spherical nanoparticles, though of smaller diameters of 3.5 – 5.0 nm. Most of the nanoparticles were present as large aggregates, and few were adsorbed on the surface of the silica. In this sense, the current catalysts may be considered ‘mixed agglomerated catalysts’, as described by Perego and Villa [38].

Analysis of the halloysite showed it shared characteristics with both of the previous support materials. The particles were small clusters 12.7 ± 7.6 μm in diameter, each composed of a mixture of tubules and platelets. Relatively few macroscopic aggregates of metal were observed, with most of the nanoparticles present distributed around the edges of the support particles which had the platelet morphology. All of the nanoparticles were spherical in morphology. Few particles were found adsorbed on the tubules, and those which did were found exclusively on their outsides. The average particle size ranged from 3.2 nm – 8.3 nm depending on the metal, though no such trend was observed in the spatial distribution of the particles. The size and clustering of the particles is similar to that reported by Rostamzadeh *et al.* who prepared Au/HNC catalysts using a similarly simple synthetic method, though the locations of the nanoparticles are different between their study and ours [39]; while their catalysts contained many particles within the interior of the tubules, ours contained none.

3.3 X-Ray Powder Diffraction

Powder diffraction analysis of the alumina produced a pattern with a low, flat background, and a series of narrow diffraction peaks corresponding in position to $\alpha\text{-Al}_2\text{O}_3$ (ICDD PDF 01-077-2135). In the case of the alumina-supported catalysts, the patterns additionally contained five diffraction peaks corresponding to metallic rhodium (ICDD PDF 00-001-1214), palladium (ICDD PDF 01-071-3757), or platinum (ICDD PDF 01-071-3756). Line broadening analysis of the metal peaks gave average particle sizes of 7.3 nm – 9.2 nm, except for the Rh/ Al_2O_3 system for the diffraction peaks were too wide to be reasonably analysed. These values are shown in Table 2, along with the sizes derived from TEM data. This illustrates that at least some of the metal within the systems is in the zero-valent metallic form, rather than as oxides such as PdO, Rh_2O_3 , or PtO_2 .

Analysis of the silica-based systems all gave similar results, exhibiting a weak and broad background peaking at $22^\circ 2\theta$ and tailing off toward higher angles. The systems containing nanoparticles clearly exhibited the same metal peaks as observed in the alumina-based systems, but were significantly narrower and could be easily resolved from the background. The particle sizes calculated from line broadening analysis for these systems ranged from 4.0 nm – 7.3 nm.

The diffraction pattern of the pristine halloysite was different again from both the silica and alumina, exhibiting a series of slightly broadened peaks characteristic of partially disordered clay minerals, and similar to previously reported halloysite diffraction patterns [40-42]. The diffraction patterns of the halloysite-supported metals contained the same identical sets of peaks as the support, but once again contained the additional peaks corresponding to metallic Rh, Pd, and Pt. The calculated particle sizes in these instances ranged from 3.0 – 5.2 nm.

3.4 Solid-State Nuclear Magnetic Resonance Spectroscopy

The pristine silica, as received, exhibited three resonances in the ^1H - ^{29}Si CPMAS spectrum at -91.3 ppm, -101.2 ppm, and -110.6 ppm, corresponding respectively to silicon atoms with two attached silanols ('Q² sites'), one attached silanol ('Q³ sites'), and no attached silanols ('Q⁴ sites'). This pattern is typical of silica gels reported in the literature, especially those of high surface area [43]. The ^1H spectrum exhibited a broad resonance at 4.4 ppm (adsorbed water) and two sharp resonances at 3.6 ppm (H-bonded silanols) and 1.1 ppm (free silanol groups) [44]. No significant changes were observed in the ^{29}Si spectra after immobilisation of nanoparticles, though the ^1H spectra showed several key changes: the water peak was significantly weaker and narrower than for the pristine support, and the peaks for the surface silanols disappeared entirely. This is illustrated in Figure 3. This suggests that the preparative procedure largely dehydrates the surface of the silica, while silanols present in the bulk remain unaffected.

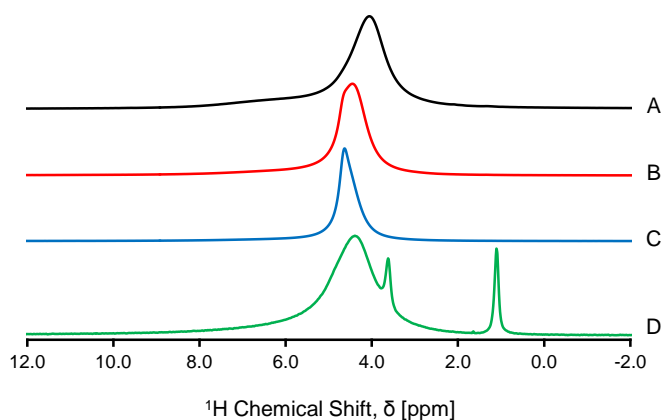


Figure 3: ^1H solid-state NMR spectra of the silica-supported catalysts, corresponding to Rh/SiO₂ (A), Pd/SiO₂ (B), Pt/SiO₂ (C), and pristine SiO₂ (D)

The ^{27}Al DPMAS spectra of the pristine alumina exhibited a single broad symmetric resonance at 9.8 ppm (FWHM 12.4 ppm) corresponding to octahedral AlO₆ environments [45]. Spectra of the alumina-supported catalysts produced similar spectra, but with some subtle changes to the line shapes at *ca.* -75 ppm, the region of spectral space corresponding to tetrahedral AlO₄ units adjacent to octahedral AlO₆ units. As this is not a structural motif which $\alpha\text{-Al}_2\text{O}_3$ formally contains, it is most likely associated with regions in the material at which significant crystallographic distortions may occur, for example the surfaces of the particles. Adsorption of nanoparticles to these surfaces would then produce changes to the coordination of the alumina atoms, and changes to the structure of the resonances. This is precisely what was observed, and is shown in Figure 4.

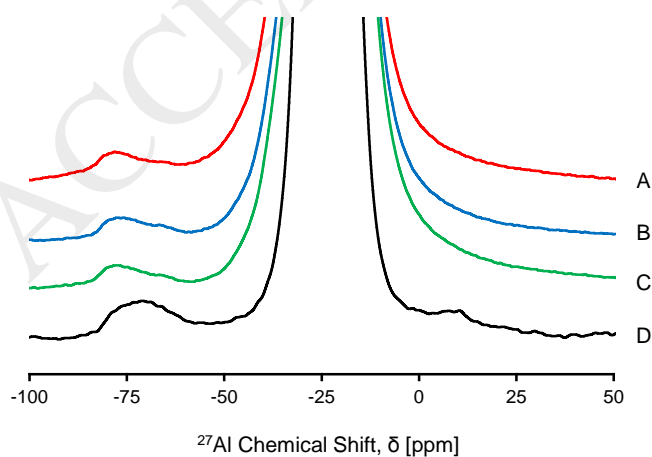


Figure 4: ^{27}Al NMR spectra of the alumina-based systems. The four plots correspond to Rh/ Al_2O_3 (A), Pd/ Al_2O_3 (B), Pt/ Al_2O_3 (C), and pristine Al_2O_3 (D). All spectra are scaled to equal relative intensity.

The halloysite, as received, exhibited two overlapping resonances in the ^1H spectrum of nearly equal intensity, corresponding to silanol and aluminol resonances. A single resonance at -28 ppm (19.6 ppm FWHM) was observed in the ^{27}Al DPMAS spectrum, tailing toward higher field. This is similar to previously reported spectra, and originates from halloysite's structural AlO_6 units⁴⁷. The ^1H - ^{29}Si CPMAS spectrum contained only a single resonance at -92.8 ppm (2.5 ppm FWHM), while the ^{29}Si DPMAS spectrum contained an additional resonance at -108.9 ppm (1.2 ppm FWHM) with a relative intensity of ca. 5%. Immobilisation of nanoparticles on the halloysite produced an array of effects. Though no significant changes were observed in either of the ^{29}Si CPMAS or DPMAS spectra, the ^1H DPMAS spectra showed a clearly diminished aluminol resonance, and the ^{27}Al DPMAS spectra showed the appearance of a weak shoulder at ca. 25 ppm, as shown in Figure 5. This suggests that the interaction of the metal particles with the halloysite occurs at the alumina-rich surface of the particles, rather than the silica-rich surface.

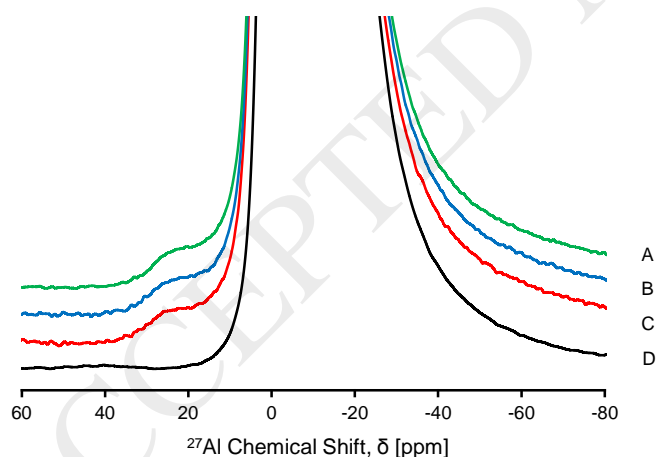


Figure 5: ^{27}Al solid-state NMR spectra of the halloysite-supported catalysts, corresponding to Pt/HNC (A), Pd/HNC (B), Rh/HNC (C), and pristine HNC (D). The resonance at 25 ppm, a shoulder off the main peak, is significantly different in A-C compared to D.

3.5 Fourier Transform Infrared Microspectroscopy

Spectra of the pristine silica contained exhibited a set of absorbance bands broadly consistent with those in the literature [46-48], but with slightly different peak shapes than are observed in traditional transmission spectra. This is due to the more complex optical path taken during infrared transfection [49, 50]. Example spectra are shown in Figure 6.

At the high energy end of the spectrum, a broad peak at 3400 cm^{-1} is observed which corresponds to hydrogen-bonded surface hydroxyls, with a shoulder at 3740 cm^{-1} corresponding to isolated hydroxyls. The broad peak is slightly narrowed when nanoparticles are adsorbed, while the shoulder remains unaffected. This can be interpreted as a reduction in the degree of hydration at the surface of the silica, which is consistent with the observations made by NMR. At the low-energy end of the spectrum there are two regions which are subtly different between the pristine silica and the catalysts. At $700\text{-}1000\text{ cm}^{-1}$ there is change in the shape of the peaks, which is the spectral region corresponding to Si-O-H bending and Si-O stretching modes [51]. This is unlikely to be due to an interaction with the nanoparticles as these systems have a low surface coverage, and is thus more probably associated with the reduction in surface hydration.

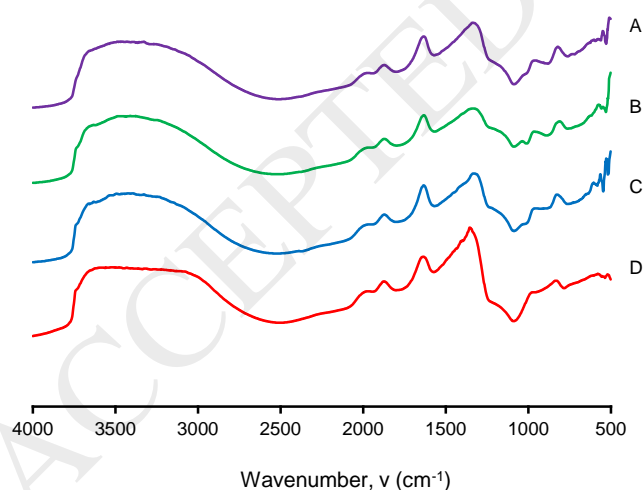


Figure 6: MicroFTIR spectra of the silica-supported catalysts, corresponding to Pt/SiO₂ (A), Pd/SiO₂ (B), Rh/SiO₂ (C), and pristine SiO₂ (D). The Y axis is shown in absorbance mode, and spectra are artificially offset for clarity.

Spectra of the pristine alumina were also similar to those in the literature, and showed significant differences between those collected *via* transmission or transflection methods. Transmission spectra were mostly featureless except below 1000 cm^{-1} , where overlapping bands corresponding to AlO_6 bending, stretching, and mixed surface modes are observed but are largely irresolvable from one another [52, 53]. Comparatively, the transflection spectra showed clearer definition of these peaks, especially at 1050 cm^{-1} (Al-O-H bend), 820 cm^{-1} (surface mode), and 630 cm^{-1} (Al- O_6 stretch) [52]. The enhancement of these features in the transflection spectra is most likely due to their association with the surface of the alumina particles, which has been observed in a previous study on infrared reflectance [54].

When nanoparticles were immobilised onto the alumina there significant changes evident in the transflection spectra. Several features disappeared, including a broad band centred around 3400 cm^{-1} (water O-H stretch), a sharper peak at 3295 cm^{-1} (surface AlO-H stretches), and the two bands around 1500 cm^{-1} (adsorbed water bends) [55]. At the same time, some subtle distortions are evident around 650 cm^{-1} , which together suggest that the surface of the alumina is becomes dehydrated and slightly strained. Given the high surface coverage of nanoparticles this is unsurprising, and is supported by the NMR data. Example spectra are shown in Figure 7.

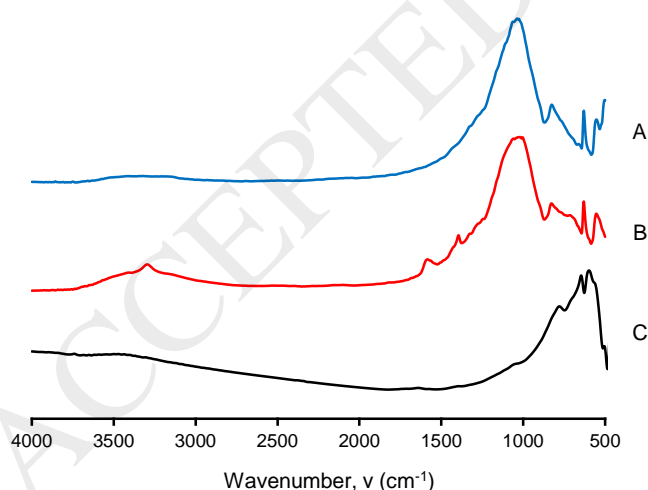


Figure 7: FTIR spectra of pristine Al_2O_3 by KBr transmission (A), pristine Al_2O_3 by microspectroscopy (B) and $\text{Pd}/\text{Al}_2\text{O}_3$ by microspectroscopy (C). The Y axis is shown in absorbance mode, and spectra are artificially offset for clarity.

The spectra of halloysite were far more complex than either of the other materials, though with similarities to both. At the high energy end of the spectra three sharp peaks were observed at 3700 cm^{-1} , 3628 cm^{-1} , and 3552 cm^{-1} , corresponding to O-H stretches of three different types of surface hydroxyl [41]. Progressing toward lower energy, two sets of peaks are evident at $1500\text{--}2000\text{ cm}^{-1}$ (adsorbed water) analogous to both alumina and silica, before reaching a complex ‘fingerprint region’ below 1200 cm^{-1} . Immobilisation of nanoparticles to the halloysite caused an array of distortions in the fingerprint region of the spectrum, especially in the region around 1000 cm^{-1} assigned in alumina as being due to surface modes, but no changes to any of the other features in the spectra. This suggests that the interaction between the halloysite and the nanoparticles is not mediated through surface hydroxyls, but via an interaction with the alumina-rich edges of the material. Example spectra are shown in Figure 8

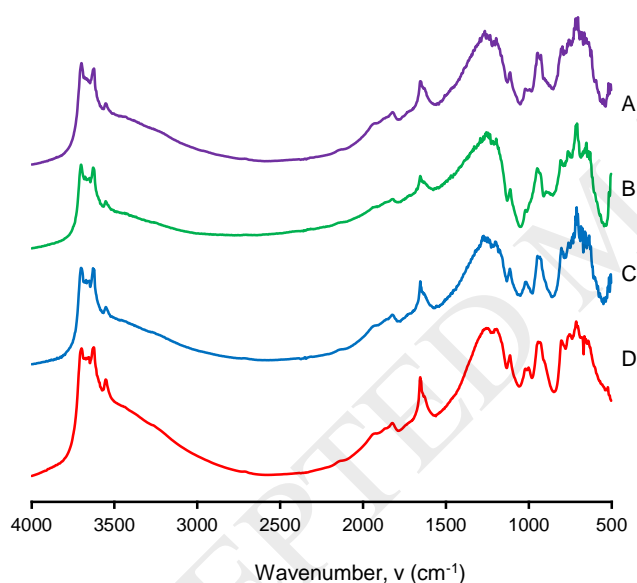


Figure 8: MicroFTIR spectra of the halloysite systems, Pt/HNC (A), Pd/HNC (B), Rh/HNC (C), and pristine HNC (D). The Y axis is shown in absorbance mode, and spectra are artificially offset for clarity.

4. Discussion

It is clear from a cursory analysis of the data that these materials exhibit significant catalytic activity, beyond that of the pristine support materials. This activity is not surprising, as precious metal nanoparticles are known as potent hydrogenation catalysts. Of significant interest is

difference in the extent of activity between the systems, and the correlations which can be drawn with the spectroscopic data.

By far the greatest catalytic activity observed in this study was with the halloysite-supported systems. In the case of octene hydrogenation, conversion rates of several hundred $\mu\text{mol hr}^{-1} \text{g}^{-1}$ were maintained by the Pd/HNC catalyst for more than an hour, which corresponded to 100% substrate conversion during this period. If the number of active sites in the catalysts are estimated using the method of Borodziński and Bonarowska [56], and then used to calculate turnover frequencies [57], activities in excess of 30,000 hr^{-1} are obtained. A full tabulation of TOFs calculated in this fashion is given in Table 3. These compare favourably to what is reported in the literature, especially as the current reactions were performed under ambient conditions. While these are a limited set of results, they further support that halloysite is a viable support material to use for the preparation of supported catalysts. Comparatively, the alumina and silica-supported catalysts displayed activities of less than half of these values. As no mass-transfer tests were conducted in this set of experiments, it is possible that these may be conservative estimates and that selected values could be increased further by optimising the experimental conditions.

Table 3: Calculated turnover frequencies (TOF) of the thirty-six systems studied herein. All rates are given to two significant figures.

Catalyst	Calculated TOF (hr^{-1})		
	Cyclohexene	1-Octene	1,4-Cyclooctadiene
Rh/SiO ₂	4,400	16,000	3,200
Rh/Al ₂ O ₃	1,000	7,200	1,500
Rh/HNC	5,600	24,000	6,100
Pd/SiO ₂	2,900	10,000	2,800
Pd/Al ₂ O ₃	5,400	40,000	6,200
Pd/HNC	16,000	55,000	11,000
Pt/SiO ₂	4,400	12,000	1,200
Pt/Al ₂ O ₃	1,700	6,500	610
Pt/HNC	13,000	25,000	2,000

The most likely cause of the differences in activity between systems is the morphological properties of the supported metal particles. Other factors being equal, a greater activity should be obtained when a greater surface area of metal is exposed, which arises with small particle sizes as well as a homogeneous spatial distribution of metal particles across the support. In the case of the presently reported systems, no statistically significant difference in particle size was detected between the three support materials using ANOVA ($F(2,6)=0.29$, $P=0.76$), suggesting particle size is not the cause of the differences.

Spatial distribution data obtained *via* electron microscopy suggested the metal distribution was the most homogeneous in the halloysite-supported catalysts, and the least homogeneous in the silica catalysts, which correlates with the observed activities. The question thus arises why the metal distribution is better throughout the halloysite catalysts. As the immobilisation occurred selectively at the edges of the particles, the mechanism must be related to structural motifs uniquely present at these sites. These are the positions at which lattice defects would most likely occur, producing absorption sites where interactions between the halloysite support particles and the metal nanoparticles could occur. These may be acid-base or electrostatic type interactions, and further work would be required to elucidate the relative contributions of the two [1, 58].

Though the observations of metal distribution are qualitative, they are supported by changes observed in the spectroscopic data. The alumina-based systems showed evidence of surface perturbation in both the FTIR and NMR spectra upon the immobilisation of nanoparticles, which is consistent with the high degree of surface coverage observed by electron microscopy. Conversely, the silica-based systems showed less evidence of surface changes aside from dehydration, which is also consistent with the low degree of surface coverage of metal particles. The halloysite-based systems exhibited some of the most significant changes to the surface chemical resonances or adsorption bands, which once more, is consistent with the good surface coverage and low levels of aggregation observed by electron microscopy.

Interestingly, the spectroscopic data for the halloysite catalysts showed changes to the alumina-specific regions of the FTIR spectra and the ^{27}Al NMR spectra, though no such changes were observed to the silica-specific spectra. This suggests that this method results in

preferential adsorption of nanoparticles to the alumina-rich faces of the halloysite particles. This was essentially confirmed by electron microscopy, which showed that the metal particles were primarily located at the edges of the flat halloysite platelets, rather than on the interior of the tubules. In the future, it is therefore important to consider which morphology is preferential – though the use of nanotubules is attractive, it may not necessarily be the most effective as a support material. Most studies using halloysite as a support material, including nearly all of those referenced in this manuscript, use the tubular variety of halloysite, though our study suggests that better results may be obtained using other morphologies, depending on the nature of the synthetic method used.

Another possibility which may have affected the activities is the presence of residual lanthanum in the systems, which was used to destabilise the colloidal material present. Lanthanum [59], along with many other lanthanides [60-62], are known to promote catalytic hydrogenations. It is likely that a similar effect has occurred in the catalysts described in this research, though the effect is most pronounced in the halloysite catalysts due to their better spatial distribution of metal than the other catalysts studied. The concept is exciting regardless, as it suggests that the activity of the catalysts could be further improved by varying the identity, concentration, or distribution of the lanthanide within the catalysts.

In the future, it would be of interest to develop methods to improve the distribution of the metal particles, both on halloysite and other support materials. Clearly the synthetic method used herein is viable, but produces catalysts with varying degrees of metal aggregation depending on the nature of the support. This in turn carries through to the observable catalytic activity of the systems, making comparisons between systems difficult. Regardless, taken “as is”, it can give rise to halloysite-supported catalysts with exceptional activity.

5. Conclusions

We have shown for the first time that highly active halloysite-supported metal catalysts can be prepared by a simple one-pot reduction method. The resulting catalysts displayed excellent activity in the hydrogenation of a range of olefins at standard temperature and pressure, with conversion rates of up to $340 \mu\text{mol hr}^{-1} \text{g}^{-1}$ (or $55,000 \text{ hr}^{-1}$ as a TOF) for the hydrogenation of 1-octene by halloysite-supported palladium nanoparticles. In all instances the halloysite-

supported catalysts displayed superior catalytic and properties to equivalent catalysts prepared using the more traditional support materials alumina and silica. Characterisation of the materials showed that the halloysite-supported catalysts had the most favourable textural properties, with the most even dispersion of metal across their surfaces, though a tendency toward immobilisation on the alumina-rich edges of particles. This shows that while nanotubular halloysite may seem the most attractive option as a catalyst support, better metal distribution may be obtained with other morphologies. Further work should be undertaken to optimise the activity of these catalysts, and investigate their activity in a range of other catalytic reactions.

6. Acknowledgements

JEJ and MRM thanks Imerys for the generous donation of halloysite. JEJ additionally thanks the University of Waikato for the provision of a doctoral scholarship during the course of this work.

References

1. E. Joussein *et al.*, *Clay Miner.*, 40(4), **2005**, 383-426
2. M. Soma, G. J. Churchman, B. K. G. Theng, *Clay Miner.*, 27(4), **1992**, 413-421
3. G. J. Churchman, T. J. Davy, L. A. G. Aylmore, R. J. Gilkes, P. G. Self, *Clay Miner.*, 30(2), **1995**, 89-98
4. R. L. Brathwaite, A. B. Christie, K. Faure, M. G. Townsend, S. Terlesk, *Miner. Deposita*, 47(8), **2012**, 897-910
5. G. Lazzara *et al.*, *Curr. Opin. Colloid Interface Sci.*, 35, **2018**, 42-50
6. Y. Zhang, A. Tang, H. Yang, J. Ouyang, *Appl. Clay Sci.*, 119, **2016**, 8-17
7. S. R. Levis, P. B. Deasy, *Int. J. Pharm.*, 243(1-2), **2002**, 125-134
8. Y. M. Lvov, D. G. Shchukin, H. Möhwald, R. R. Price, *ACS Nano*, 2(5), **2008**, 814-820
9. M. Du, B. Guo, D. Jia, *Polym. Int.*, 59(5), **2010**, 574-582
10. M. Zou *et al.*, *Mater. Res. Bull.*, 61(0), **2015**, 375-382
11. M. Massaro *et al.*, *J. Mater. Chem. A*, 5(26), **2017**, 13276-13293
12. T. Tsoufis *et al.*, *Chem. Eng. J.*, 313, **2017**, 466-474
13. L. Gómez, J. L. Hueso, M. C. Ortega-Liébaná, J. Santamaría, S. B. Cronin, *Catal. Commun.*, 56(0), **2014**, 115-118
14. X. Zeng, Q. Wang, H. Wang, Y. Yang, *J. Mater. Sci.*, 52(14), **2017**, 8391-8400
15. M. Malmir, M. M. Heravi, S. Sadjadi, T. Hosseinejad, *Appl. Organomet. Chem.*, 32(4), **2018**, e4291
16. V. A. Vinokurov *et al.*, *ACS Sustain. Chem. Eng.*, 5(12), **2017**, 11316-11323
17. V. Vinokurov *et al.*, *Ind. Eng. Chem. Res.*, 56(47), **2017**, 14043-14052
18. A. Philip, J. Lihavainen, M. Keinänen, T. T. Pakkanen, *Appl. Clay Sci.*, 143, **2017**, 80-88
19. M. Massaro *et al.*, *RSC Advances*, 6(60), **2016**, 55312-55318
20. Q. Wei, R. Shi, D. Lu, Z. Lei, *RSC Advances*, 6(35), **2016**, 29245-29253
21. C. Li, X. Li, X. Duan, G. Li, J. Wang, *J. Colloid Interface Sci.*, 436, **2014**, 70-76
22. Y. Zhou *et al.*, *J. Clean. Prod.*, 103, **2015**, 925-933
23. S. Mandal, D. Roy, R. V. Chaudhari, M. Sastry, *Chem. Mater.*, 16(19), **2004**, 3714-3724
24. P. Gallezot, A. Giroir-Fendler, D. Richard, *Catal. Lett.*, 5(2), **1990**, 169-174
25. J. Geboers, S. Van de Vyver, K. Carpentier, P. Jacobs, B. Sels, *Chem. Commun.*, 47(19), **2011**, 5590-5592
26. R. V. Malyala, C. V. Rode, M. Arai, S. G. Hegde, R. V. Chaudhari, *Appl. Cat. A: Gen.*, 193(1), **2000**, 71-86

27. P. Munnik, P. E. de Jongh, K. P. de Jong, *Chem. Rev.*, 115(14), **2015**, 6687-6718
28. D. N. Furlong, A. Launikonis, W. H. F. Sasse, J. V. Sanders, *J. Chem. Soc. Faraday Trans.*, 80(3), **1984**, 571-588
29. J. E. Jaine, M. R. Mucalo, *Powder Technol.*, 276(0), **2015**, 123-128
30. D. Balzar *et al.*, *J. Appl. Crystallogr.*, 37(6), **2004**, 1-14
31. E. E. Gonzo, M. Boudart, *J. Catal.*, 52(3), **1978**, 462-471
32. O. Domínguez-Quintero *et al.*, *J. Mol. Catal A Chem.*, 197(1-2), **2003**, 185-191
33. L. M. Rossi *et al.*, *Green Chem.*, 9(4), **2007**, 379-385
34. M. Boudart, D. J. Sajkowski, *Faraday Discuss.*, 92(0), **1991**, 57-67
35. M. Adlim, M. Abu Bakar, K. Y. Liew, J. Ismail, *J. Mol. Catal A Chem.*, 212(1-2), **2004**, 141-149
36. G. Deganello, D. Duca, A. Martorana, G. Fagherazzi, A. Benedetti, *J. Catal.*, 150(1), **1994**, 127-134
37. R. L. Augustine, F. Yaghmaie, J. F. Van Peppen, *J. Org. Chem.*, 49(11), **1984**, 1865-1870
38. C. Perego, P. Villa, *Catalysis Today*, 34(3-4), **1997**, 281-305
39. T. Rostamzadeh *et al.*, *Langmuir*, 33(45), **2017**, 13051-13059
40. D. Banaś *et al.*, *Radiat. Phys. Chem.*, 93(0), **2013**, 129-134
41. B. Szczepanik *et al.*, *J. Mol. Struct.*, 1084(0), **2015**, 16-22
42. G. Tarì, I. Bobos, C. S. F. Gomes, J. M. F. Ferreira, *J. Colloid. Interf. Sci.*, 210(2), **1999**, 360-366
43. D. W. Sindorf, G. E. Maciel, *J. Am. Chem. Soc.*, 105(6), **1983**, 1487-1493
44. C. E. Bronnimann, R. C. Zeigler, G. E. Maciel, *J. Am. Chem. Soc.*, 110(7), **1988**, 2023-2026
45. K. J. D. MacKenzie, M. E. Smith, *Multinuclear Solid-State NMR of Inorganic Materials* (Elsevier Science Ltd., Oxford, 2002)
46. A. J. Van Roosmalen, J. C. Mol, *J. Phys. Chem.*, 83(19), **1979**, 2485-2488
47. A. J. Van Roosmalen, J. C. Mol, *J. Phys. Chem.*, 82(25), **1978**, 2748-2751
48. E. I. Kamitsos, A. P. Patsis, G. Kordas, *Phys. Rev. B*, 48(17), **1993**, 12499-12505
49. B. J. Davis, P. S. Carney, R. Bhargava, *Anal. Chem.*, 82(9), **2010**, 3487-3499
50. B. J. Davis, P. S. Carney, R. Bhargava, *Anal. Chem.*, 82(9), **2010**, 3474-3486
51. H. A. Benesi, A. C. Jones, *J. Phys. Chem.*, 63(2), **1959**, 179-182
52. A. Boumaza *et al.*, *J. Solid State Chem.*, 182(5), **2009**, 1171-1176
53. L. Favaro *et al.*, *J. Solid State Chem.*, 183(4), **2010**, 901-908
54. A. S. Barker, *Physical Review*, 132(4), **1963**, 1474-1481

55. P. Jackson, G. D. Parfitt, *Trans. Faraday Soc.*, 67(0), **1971**, 2469-2483
56. A. Borodziński, M. Bonarowska, *Langmuir*, 13(21), **1997**, 5613-5620
57. M. Boudart, *Chem. Rev.*, 95(3), **1995**, 661-666
58. P. Yuan, D. Tan, F. Annabi-Bergaya, *Appl. Clay. Sci.*, 112-113, **2015**, 75-93
59. Y.-z. Xiang, L.-n. Kong, C.-s. Lu, L. Ma, X.-n. Li, *React. Kinet. Mech. Catal.*, 100(1), **2010**, 227-235
60. H. Imamura, M. Yoshinobu, T. Mihara, Y. Sakata, S. Tsuchiya, *J. Mol. Catal.*, 69(2), **1991**, 271-280
61. J. T. Lee, H. Alper, *J. Org. Chem.*, 55(6), **1990**, 1854-1856
62. H. Imamura, K. Igawa, Y. Kasuga, Y. Sakata, S. Tsuchiya, *J. Chem. Soc., Faraday Trans.*, 90(14), **1994**, 2119-2124